Optics Letters

Measuring nonclassicality with silicon photomultipliers

Giovanni Chesi,[1,2] Luca Malinverno,[1] Alessia Allevi,[1,2] Romualdo Santoro,[1] Massimo Caccia,[1] and Maria Bondani[2,*]

[1]Department of Science and High Technology, University of Insubria, Via Valleggio 11, I-22100 Como, Italy
[2]Institute for Photonics and Nanotechnologies, CNR, Via Valleggio 11, I-22100 Como, Italy
*Corresponding author: maria.bondani@uninsubria.it

Received 5 October 2018; revised 6 February 2019; accepted 9 February 2019; posted 11 February 2019 (Doc. ID 341271); published 7 March 2019

Detector stochastic deviations from an ideal response can hamper the measurement of quantum properties of light, especially in the mesoscopic regime where photon-number resolution is required. We demonstrate that, by proper analysis of the output signal, nonclassicality of twin-beam states can be detected and exploited with commercial and cost-effective silicon-based photon-number-resolving detectors.

https://doi.org/10.1364/OL.44.001371

Quantum features of optical states are often fragile, and their measurement requires advanced detection schemes to achieve sufficient quantum efficiency, low noise, no spurious effects, and photon-number resolution. This holds both in the case of single-photon states [1] and in the case of mesoscopic states [2,3]. That is why quantum optics has triggered research on new photon-number-resolving (PNR) detectors, especially in the past 20 years [4–7]. Among PNR detectors, silicon photomultipliers (SiPMs, also known as multi-pixel photon counters), introduced in late 1990s [8–12], feature photon-number resolution, wide dynamic range, reasonable quantum efficiency (up to 60% in the visible spectral range), and room temperature operability, which make them potentially attractive for quantum optics applications. Nevertheless, the presence of spurious effects has so far [13,14] prevented their exploitation in quantum optics. On the contrary, SiPMs have found a large use for particle-physics experiments and for positron-emission tomography [15]. SiPMs consist of a matrix of avalanche photodiodes connected in parallel to a single output. Each diode is reverse-biased at a voltage value exceeding the breakdown threshold, and it works in Geiger Müller regime, yielding a standard output signal at any detection event. The number of active cells results in an output signal proportional to the overall number of detected photons. In addition to the signal generated by the impinging light, the output also includes dark counts, crosstalks, and afterpulses. The dark-count rate can be decreased by lowering the temperature, while crosstalk and afterpulse probabilities depend mainly on detector architecture and technology. In the present generation of SiPMs, the crosstalk probability has been lowered to few percent, and the afterpulses are almost negligible.

In spite of the high quality of the detectors, the residual imperfections can still severely affect the measurement of quantum features of optical states.

To minimize their influence, we can take advantage of the different temporal occurrences of the spurious effects with respect to the light signal. Dark counts are randomly distributed in time, while crosstalk and afterpulse events are triggered by detection events and thus can occur at a delayed time with respect to the primary detection. As an example, in Fig. 1, we show typical SiPM outputs containing some delayed events. By properly choosing the temporal acquisition gate centered around the peak synchronous with the light pulses (see the different windows in the figure), we can get rid of the contribution of non-synchronous events.

We consider the experimental setup in Fig. 2, in which mesoscopic twin beam (TWB) states are generated by parametric downconversion (PDC) in type-I quasi-collinear interaction geometry. The pumping field is the fourth harmonics of a Nd:YLF laser (4.5-ps pulse duration and 500-Hz repetition rate), while the nonlinear material is a β-barium-borate (BBO) crystal (BBO2, cut angle = 46.7 deg, 6 mm long).

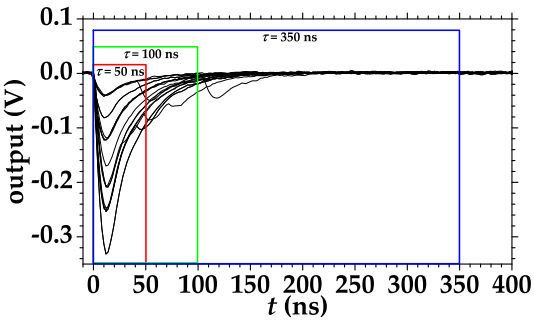

Fig. 1. Typical SiPM outputs in which delayed spurious events are visible. In the figure, the three windows centered around the peak correspond to different integration gates: 50-ns gate (red), 100-ns gate (green), and 350-ns gate (blue).

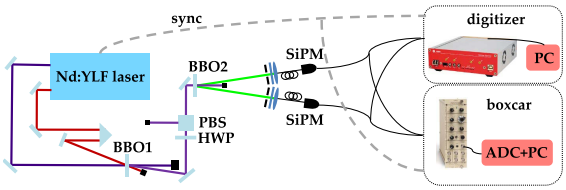

Fig. 2. Experimental setup for the measurement of multimode TWB states.

The generated TWB state is intrinsically multimode [17] and the photon-number statistics of each of the two parties is well described by multimode thermal distribution. Two portions of TWB around frequency degeneracy (523 nm), spatially and spectrally filtered by means of two variable irises and two bandpass filters, are delivered to the sensors via two multimode optical fibers (600-μm core diameter). In the experimental conditions under investigation, the effective number of independent thermal modes is larger than 100 [3], so that the photon statistics closely resembles a Poissonian distribution, with a Fano factor $F \simeq 1$. The state characterization is performed as a function of pump intensity, which is modified through a half-wave plate (HWP) followed by a polarizing cube beam splitter (PBS). For each energy value, 10^5 single-shot acquisitions are performed by using two SiPMs (MPPC S13360-1350CS, Hamamatsu Photonics). In order to devise the best signal acquisition strategy, we implemented simultaneous acquisition of the detector outputs by two different acquisition systems. According to Fig. 2, the electronic signal from the two SiPM detectors was split in two and sent to two synchronous boxcar-gated integrators (SR250, Stanford Research Systems) and to a desktop waveform digitizer (DT5720, CAEN) operating at 12-bit resolution and at 250-MS/s sampling rate. The boxcar integrator performs an analogical integration of the signal over gates of variable widths centered on the signal peak. For comparison between the acquisition chains, we set the gate width of the boxcar at $\tau = 50$ ns, while the output of the digitizer is integrated off-line over different time gates, $\tau = 50, 100, 350$ ns. We note that the gate width can be pushed down to 10 ns for the boxcar, while to have a reasonable number of points in the integral, the minimum gate for the digitizer is 50 ns.

As a test of nonclassicality for the TWB state, we consider the noise reduction factor in the two arms of the TWB [18]. In the case of SiPMs, which are affected by crosstalk and dark counts, the detection output is given by the number of detected photons increased by the dark counts and by the crosstalk. Following the model of the detector in Ref. [19], we call k the binned output (once binned in integer values, k is integer, noting that $\langle k\rangle = (1+\varepsilon)(\eta\langle n\rangle + \langle m_{\rm dc}\rangle)$, $\langle n\rangle$ being the mean number of photons in each of the two arms of the TWB, η the detector quantum efficiency, ε the crosstalk probability, and $\langle m_{\rm dc}\rangle$ the mean value of dark counts. The measured noise reduction factor is thus

$$R = \frac{\sigma^2(k_1 - k_2)}{\langle k_1\rangle + \langle k_2\rangle}, \tag{1}$$

where $\sigma^2(\cdot)$ denotes the variance, and k_j are measured shot-by shot in the two arms of the TWB. It is well known that the condition $R < 1$ is sufficient for nonclassicality. In Fig. 3, we plot the measured values of R as a function of $\langle k\rangle = (\langle k_1\rangle + \langle k_2\rangle)/2$. The different colors in the figure correspond to different gate widths (see caption for details). In order to superimpose a proper theoretical expectation on the experimental data, we derived a model that takes into account the nonidealities of SiPMs, i.e., the non-unitary quantum efficiency and the crosstalk and dark-count effects, whose statistical properties have been already described in [16]. The most general expression for R obtained by measuring a multimode TWB state composed by μ equally populated modes is

$$R = 1 + \frac{1}{\mu}\frac{(\langle k_1\rangle - \langle k_2\rangle)^2}{(\langle k_1\rangle + \langle k_2\rangle)} + \frac{2\varepsilon_1}{1+\varepsilon_1}\frac{\langle k_1\rangle}{(\langle k_1\rangle + \langle k_2\rangle)} + \frac{2\varepsilon_2}{1+\varepsilon_2}\frac{\langle k_2\rangle}{(\langle k_1\rangle + \langle k_2\rangle)} - \frac{2}{\mu}[(1+\varepsilon_1)\langle m_{1\rm dc}\rangle - (1+\varepsilon_2)\langle m_{2\rm dc}\rangle]\frac{(\langle k_1\rangle - \langle k_2\rangle)}{(\langle k_1\rangle + \langle k_2\rangle)}$$
$$- \frac{2\sqrt{(1+\varepsilon_1)(1+\varepsilon_2)\eta_1\eta_2(\langle k_1\rangle - (1+\varepsilon_1)\langle m_{1\rm dc}\rangle)(\langle k_2\rangle - (1+\varepsilon_2)\langle m_{2\rm dc}\rangle)}}{(\langle k_1\rangle + \langle k_2\rangle)} + \frac{1}{\mu}[(1+\varepsilon_1)\langle m_{1\rm dc}\rangle - (1+\varepsilon_2)\langle m_{2\rm dc}\rangle]^2, \tag{2}$$

where $j = 1, 2$ refer to the two arms of the TWB state. Equation (2) reduces to the model introduced in Ref. [14] for $\langle m_{j\rm dc}\rangle = 0$, and $\varepsilon_1 = \varepsilon_2$, $\eta_1 = \eta_2$, and $\langle k_1\rangle = \langle k_2\rangle$. Moreover, for $\langle m_{j\rm dc}\rangle = 0$ and $\varepsilon_j = 0$, Eq. (2) reduces to the expression used in Ref. [3] to describe the results with a different class of detectors. The theoretical curves in Fig. 3 have been

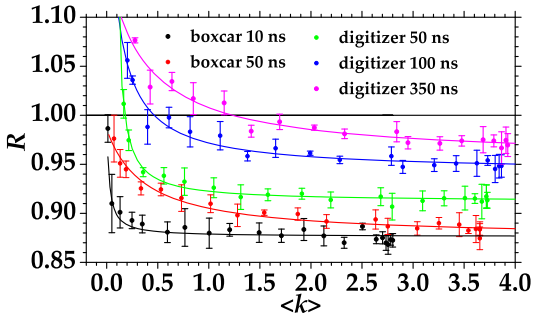

Fig. 3. Noise reduction factor R as a function of $\langle k\rangle$ for different integration gates. Full symbols: experimental data; lines: theory according to Eq. (2). With the assumption in the text, Eq. (2) takes the form $R = A + B/(x + C)$, where A and B are connected to the non-idealities of detectors, while C takes into account possible errors in the determination of the zero. In the fitting procedure, the value η determined for data with 10-ns gate width ($\eta = 0.1646 \pm 0.0004$) was used for all the other datasets. The remaining parameters are: $\varepsilon = 0.07 \pm 0.040$ (magenta), 0.062 ± 0.002 (blue), 0.0437 ± 0.0008 (green), 0.022 ± 0.002 (red), 0.0228 ± 0.0007 (black); and $\langle m_{\rm dc}\rangle = 0.06 \pm 0.02$ (magenta), 0.028 ± 0.007 (blue), 0.009 ± 0.001 (green), 0.04 ± 0.009 (red), 0.0026 ± 0.0006 (black).

evaluated according to Eq. (2) by assuming a perfect balancing between the two arms, i.e., $\langle m_{jdc}\rangle = \langle m_{dc}\rangle$, $\varepsilon_j = \varepsilon$, $\eta_j = \eta$, and $\langle k_j\rangle = \langle k\rangle$ and fitting each set of data to find η, ε, and $\langle m_{dc}\rangle$ as the free parameters. By comparing the data corresponding to the different gate widths set for the digitizer, we can argue that the shorter the gate, the lower the values of R, a result consistent with the model of the detection response [16]. Indeed at increasing integration gate, the contribution of spurious effects becomes larger and larger (see the values of the fitting parameters in the caption of Fig. 3), and deteriorates the observation of sub-shot-noise correlations. Moreover, it is clear that the boxcar-gated integrator performs better than the digitizer for the same gate width [see the comparison for $\tau = 50$ ns in Fig. 3(a), red and green data]. The reason for that is the finite sampling rate of the digitizer, which is not sufficient to reliably sample the very fast output trace in correspondence of the signal peak. To shorten the acquisition gate to the limits, in a subsequent measurement, we set the boxcar gate width to the minimum value compatible with the measurement stability, i.e., $\tau = 10$ ns. The resulting values of R, shown in Fig. 3 as black symbols, are lower than the others, thus indicating an improved capability of detecting the nonclassicality of the TWB state. This last result indicates that the cleanest information on the detected light is contained in the peak of the electronic output signal. For this reason, we implemented a peak-and-hold circuit to detect the peak value of the electronic output signal. The circuit consists of a low-noise shaping amplifier that allows a full digital peak capture procedure with a 500-MS/s digitizer. More technical details about the device can be found in Ref. [16]. In Fig. 4, we show preliminary results for the values of R as a function of $\langle k\rangle = (\langle k_1\rangle + \langle k_2\rangle)/2$ measured with the peak-and-hold apparatus (red) compared to those measured with the boxcar at $\tau = 10$ ns (black). We note that the use of the peak and hold improves the performance of the digitizer, but still gives worse results in comparison with the analogical boxcar-gated integrator. Further improvement of the peak-and-hold acquisition system is necessary to assess the limit of such technology.

Once demonstrating the nonclassical nature of the correlations between the parties of the TWB state, we can exploit it to prepare single-beam nonclassical states by conditioning operations [17,20–24]. The conditioning protocol consists of choosing one value of the output, k_{cond}, measured on one of the two

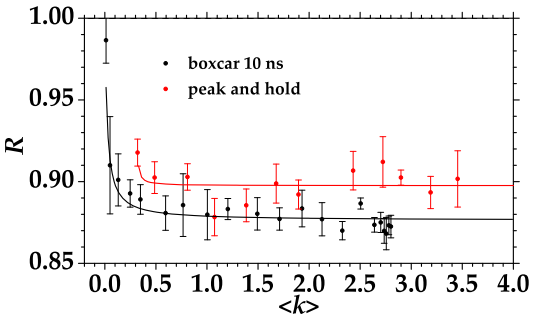

Fig. 4. Noise reduction factor R as a function of $\langle k\rangle$: peak-and-hold (red) and minimum boxcar gate (10 ns, black). Full symbols: experimental data; lines: theoretical expectation according to Eq. (2). The values of the fitting parameters are: $\langle m_{dc}\rangle \simeq 0$ (red), 0.0026 ± 0.0006 (black); and $\varepsilon = 0.035 \pm 0.003$ (red), 0.0228 ± 0.0007 (black).

parties of the TWB state, say beam #1, and selecting the corresponding value k_2 on the other beam. In general, the conditioning operation modifies the statistics of the original state. In the present case, due to the perfect photon-number correlations in the TWB, for a perfect detection chain, we would expect the conditional generation of the Fock state $|n_{cond}\rangle$, but for real experimental schemes, we can obtain only a sub-Poissonian state. In order to quantify the sub-Poissonianity of the generated states, different quantities can be evaluated, such as the Fano factor [3,20] and the autocorrelation function of the conditional states [25]. Here we focus on the Fano factor, which, in the absence of crosstalk and dark counts, is [3]

$$F_{cond} = (1-\eta)\left[1 + \frac{1}{(\langle m_2\rangle + \mu)} \times \frac{\langle m_2\rangle (m_{cond}+\mu)(\langle m_2\rangle + \eta\mu)}{(m_{cond}+\mu)(\langle m_2\rangle + \eta\mu) - \eta\mu(\langle m_2\rangle + \mu)}\right], \quad (3)$$

where $\langle m_2\rangle$ is the mean value of detected photons in state #2 before conditioning, and m_{cond} is the conditioning value. In the present case, we do not have access to the number of detected photons, m, but only to the output values, k, which include also detector imperfections. By applying the conditioning procedure to k, we get the results in Fig. 5. In particular, Fig. 5(a) contains the measured mean values of the conditional states generated by selecting different values of k_{cond} on beam #1 for signal acquisition with the boxcar integrator on 10-ns gate width, which is the best experimental condition we could achieve. Indeed, a value of R lower-than-1 is a necessary but not sufficient condition for the generation of sub-Poissonian states [26]. The initial mean value of beam #2 is $\langle k_2\rangle = 2.52$ (horizontal line in the figure), a value for which the contribution of dark counts is negligible ($\langle m_{dc}\rangle = 0.0026$, see the caption of Fig. 3). By also considering the low value of crosstalk probability ($\varepsilon = 0.0228$), we observe that the photon statistics of the detected light [19] is unaffected by detector imperfections. We will thus compare the experimental results with the same theory developed for the case without imperfections [17,20]. Crosstalk effects must be taken into account only to define an effective value of quantum efficiency. From the value of R we get $\eta' = 1 - R = \eta(1+\varepsilon) - 2\varepsilon/(1+\varepsilon) = 0.124$. All the theoretical expectations in Fig. 5 are evaluated by using the effective value η' and the measured number of modes $\mu \simeq 2000$. As expected, the mean value of the conditional state increases or decreases according to the conditioning value. In Fig. 5(b), we plot the measured Fano factor for the same conditional states shown in panel (a). We note that the values are below 1 and consistent with the theory evaluated according to Eq. (3) (red line). The horizontal line in the figure is at the value of the Fano factor of the original beam #2 ($F = 1.00126$). Finally, Fig. 5(c) shows the statistical distribution of the detected photons for the state obtained by conditioning at $k_{cond} = 5$ (black dots) along with the original distribution on beam #2. Continuous lines in the figure are theoretical predictions [17]. Even if the value of sub-Poissonianity is quite small, the effect is present and interesting: we have obtained a mesoscopic sub-Poissonian state ($\langle k\rangle_{cond} = 2.79$). We note that similar conditioning operations performed on the data acquired by the digitizer do not perform equally well, and that the best results are obtained for the shortest gate, as expected from the results in Fig. 3.

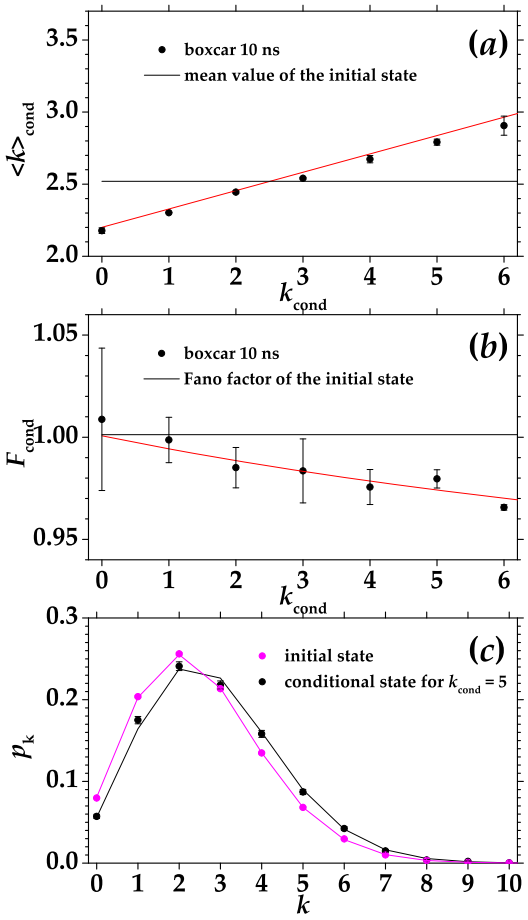

Fig. 5. (a) Mean value of the conditional states at different conditioning values; (b) Fano factor of the conditional states; (c) reconstructed photon-number statistics of unconditioned state (magenta) and conditional state (black) with $k_{cond} = 5$. The theoretical expectations are shown as lines and well superimposed to the data.

In conclusion, we have presented, for the first time to our knowledge, a detection chain based on SiPMs that can be used to test nonclassicality of mesoscopic quantum states of light. First of all, we have shown that these detectors can reveal the presence of nonclassical correlations between the two parties of a multimode TWB state. Second, we have demonstrated that they can also be used to generate and reconstruct nonclassical photon-number distributions. We notice that the intensity regimes of both the original TWB state and the conditional sub-Poissonian states are well beyond the so-called single-photon level and that the system can be operated at room temperature. Further investigations are ongoing to optimize the peak-and-hold apparatus in order to make the system as compact and portable as possible. All such features make the technology of SiPMs useful in several contexts of quantum optics and quantum information. For instance, these detectors could be used in more complex detection systems, such as in the homodyne-like detection scheme we recently implemented by means of hybrid photodetectors [27,28]. Moreover, the possibility to properly perform conditioning operations suggests the exploitation of SiPMs for tests of quantum thermodynamics [29–31].

REFERENCES

1. A. Migdall, S. V. Polyakov, J. Fan, and J. C. Bienfang, *Single-Photon Generation and Detection: Physics and Applications* (Academic, 2013), Vol. **45**.
2. M. Bondani, A. Allevi, G. Zambra, M. G. A. Paris, and A. Andreoni, Phys. Rev. A **76**, 013833 (2007).
3. A. Allevi and M. Bondani, Adv. At. Mol. Opt. Phys. **66**, 49 (2017).
4. A. E. Lita, A. J. Miller, and S. W. Nam, Opt. Express **16**, 3032 (2008).
5. G. N. Gol'tsman, O. Okunev, G. Chulkova, A. Lipatov, A. Semenov, K. Smirnov, B. Voronov, B. Dzardanov, C. Williams, and R. Sobolewski, Appl. Phys. Lett. **79**, 705 (2001).
6. J. Řeháček, Z. Hradil, O. Haderka, and J. Peřina, Jr., and M. Hamar, Phys. Rev. A **67**, 061801 (2003).
7. M. J. Fitch, B. C. Jacobs, T. B. Pittman, and J. D. Franson, Phys. Rev. A **68**, 043814 (2003).
8. A. V. Akindinov, A. N. Martemianov, P. A. Polozov, V. M. Golovin, and E. A. Grigoriev, Nucl. Instrum. Methods Phys. Res. A **387**, 231 (1997).
9. G. Bondarenko, B. Dolgoshein, V. Golovin, A. Ilyin, R. Klanner, and E. Popova, Nucl. Phys. B, Proc. Suppl. **61B**, 347 (1998).
10. V. Saveliev and V. Golutvin, Nucl. Instrum. Methods Phys. Res., Sect. A **442**, 223 (2000).
11. C. Piemonte, Nucl. Instrum. Methods Phys. Res., Sect. A **568**, 224 (2006).
12. D. Renker and E. Lorenz, J. Instrum. **4**, P04004 (2009), and references therein.
13. I. Afek, A. Natan, O. Ambar, and Y. Silberberg, Phys. Rev. A **79**, 043830 (2009).
14. D. A. Kalashnikov, S. H. Tan, T. S. Iskhakov, M. V. Chekhova, and L. A. Krivitsky, Opt. Lett. **37**, 2829 (2012).
15. P. Buzhan, B. Dolgoshein, L. Filatov, A. Ilyin, V. Kantzerov, V. Kaplin, A. Karakash, F. Kayumov, S. Klemin, E. Popova, and S. Smirnov, Nucl. Instrum. Methods Phys. Res. A **504**, 48 (2003).
16. G. Chesi, L. Malinverno, A. Allevi, R. Santoro, M. Caccia, A. Martemiyanov, and M. Bondani, "Optimizing silicon photomultipliers for quantum optics," arXiv:1812.02555 (2018).
17. A. Allevi, A. Andreoni, F. Beduini, M. Bondani, M. G. Genoni, S. Olivares, and M. G. A. Paris, Europhys. Lett. **92**, 20007 (2010).
18. A. Agliati, M. Bondani, A. Andreoni, G. De Cillis, and M. G. A. Paris, J. Opt. B Quantum Semiclass. Opt. **7**, S652 (2005).
19. M. Ramilli, A. Allevi, V. Chmill, M. Bondani, M. Caccia, and A. Andreoni, J. Opt. Soc. Am. B **27**, 852 (2010).
20. M. Lamperti, A. Allevi, M. Bondani, R. Machulka, V. Michalek, O. Haderka, and J. Peřina, Jr., J. Opt. Soc. Am. B **31**, 20 (2014).
21. J. Laurat, T. Coudreau, N. Treps, A. Maître, and C. Fabre, Phys. Rev. Lett. **91**, 213601 (2003).
22. J. Laurat, T. Coudreau, N. Treps, A. Maître, and C. Fabre, Phys. Rev. A **69**, 033808 (2004).
23. A. Ourjoumtsev, R. Tualle-Brouri, and P. Grangier, Phys. Rev. Lett. **96**, 213601 (2006).
24. T. S. Iskhakov, V. C. Usenko, U. L. Andersen, R. Filip, M. V. Chekhova, and G. Leuchs, Opt. Lett. **41**, 2149 (2016).
25. G. Chesi, A. Allevi, and M. Bondani, "Autocorrelation functions: a useful tool for both state and detector characterization," arXiv:1812.03088 (2018).
26. M. Lamperti, A. Allevi, M. Bondani, R. Machulka, V. Michalek, O. Haderka, and J. Peřina, Jr., Int. J. Quantum Inf. **12**, 1461017 (2014).
27. M. Bina, A. Allevi, M. Bondani, and S. Olivares, Opt. Express **25**, 10685 (2017).
28. S. Olivares, A. Allevi, G. Caiazzo, M. G. A. Paris, and M. Bondani, "Homodyne tomography with homodyne-like detection," arXiv:1809.00818 (2018).
29. M. D. Vidrighin, O. Dahlsten, M. Barbieri, M. S. Kim, V. Vedral, and I. A. Walmsley, Phys. Rev. Lett. **116**, 050401 (2016).
30. J. Hloušek, M. Ježek, and R. Filip, Sci. Rep. **7**, 13046 (2017).
31. Y. I. Bogdanov, K. G. Katamadze, G. V. Avosopiants, L. V. Belinsky, N. A. Bogdanova, A. A. Kalinkin, and S. P. Kulik, Phys. Rev. A **96**, 063803 (2017).